University of Bath

A geometry generation framework for contoured endwalls

Liam E Wood, Robin R Jones, Oliver J Pountney, James A Scobie, D Andrew Rees and Carl M Sangan

lew37@bath.ac.uk, r.r.jones@bath.ac.uk, o.j.pountney@bath.ac.uk, j.a.scobie@bath.ac.uk, ensdasr@bath.ac.uk, c.m.sangan@bath.ac.uk

Department of Mechanical Engineering
University of Bath
Bath, BA2 7AY
United Kingdom

ABSTRACT

The mainstream, or primary, flow in a gas turbine annulus is characteristically two-dimensional over the mid-span region of the blading, where the radial flow is almost negligible. Contrastingly, the flow in the endwall and tip regions of the blading is highly three-dimensional, characterised by boundary layer effects, secondary flow features and interaction with cooling flows. Engine designers employ geometric contouring of the endwall region in order to reduce secondary flow effects and subsequently minimise their contribution to aerodynamic loss.

Such is the geometric variation of vane and blade profiles - which has become a proprietary art form - the specification of an effective endwall geometry is equally unique to each blade-row. Endwall design methods, which are often directly coupled to aerodynamic optimisers, are widely developed to assist with the generation of contoured surfaces. Most of these construction methods are limited to the blade-row under investigation, while few demonstrate the controllability required to offer a universal platform for endwall design.

This paper presents a Geometry Generation Framework (GGF) for the generation of contoured endwalls. The framework employs an adaptable meshing strategy, capable of being applied to any vane or blade, and a versatile function-based approach to defining the endwall shape. The flexibility of this novel approach is demonstrated by recreating a

selection of endwalls from the literature, which were selected for their wide-range of contouring approaches.

1 INTRODUCTION

Interaction between the mainstream flow in a turbine annulus and the vanes and blades results in the generation of secondary flows. Secondary flow is most prominent where the vanes and blades intersect with the endwall (at the base of the profile) and at the tip (in the case of a blade). Minimising these secondary flows enhances the aerodynamic efficiency of each stage. Endwall contouring is often used to reduce secondary flow losses. An in-depth discussion of secondary flows is presented by Takeishi et al. [1]; key flow features are shown in Figure 1.
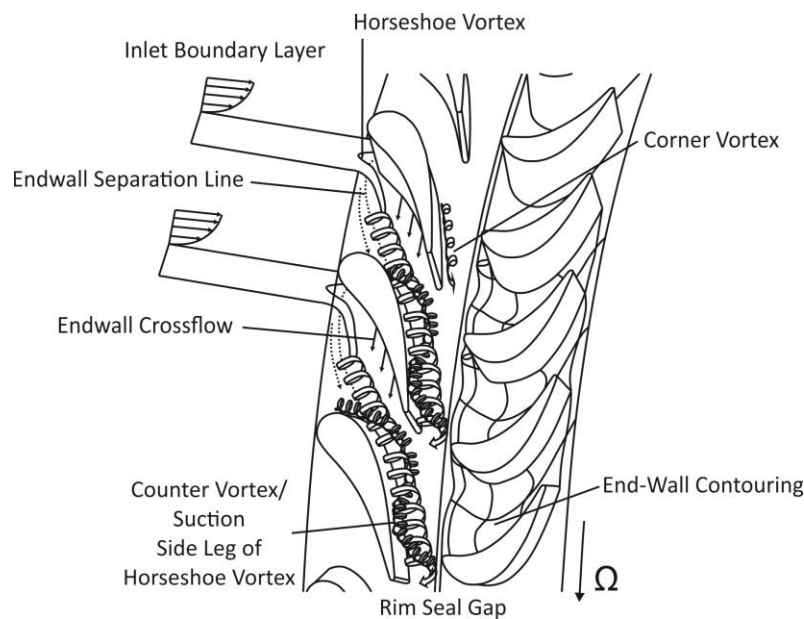
Figure 1 Secondary flow features in a turbine annulus.

The inlet boundary layer rolls up to form the horseshoe vortex at the leading edge of the aerofoil; the pressure-side leg eventually forms the core of the passage vortex. This passage vortex is a dominant secondary flow feature. Beneath the passage vortex a new boundary layer is formed on the endwall, beginning in the corner formed between the pressure side surface and the endwall.

The suction-side leg of the horseshoe vortex (often termed counter vortex) remains above the passage vortex and is forced away from the endwall as the passage vortex grows. An additional corner vortex may occur at the corner between the suction-side surface and the endwall, which rotates in the opposite direction to the passage vortex. This opposes the over-turning at the endwall, although at the cost of additional aerodynamic loss.

In addition to the losses caused directly by the secondary flows, their spanwise motion causes the exit angles of the flow to differ from the conventional 2-D design values. The passage vortex will typically cause an increase in the exit angle at the endwall (over-turning) with a compensatory reduction in angle away from the wall (under-turning). These deviations cause positive or negative incidence locally at the inlet to the next blade row and thus reduce efficiency.

Use of geometric contouring on gas turbine endwalls is an established method for reducing secondary flow losses. Each turbine blade exhibits a unique flow-field and therefore requires a customised endwall topology. Designers have successfully used non-axisymmetric EndWall Contouring (EWC) to influence the static pressure field and guide the secondary flows to reduce losses.

1.1 EWC design and parameterisation methods

The design and parameterisation methods typically employed to generate EWC geometries can be broadly categorised into three groups that depend on mathematical functions: full function-based, partially function-based and point displacement. The background to these construction methods will be discussed in turn. Alternative geometry generation methods used for the design of endwalls also exist. Some novel examples of these include Haase et al. [2], who applied an ice formation method in a linear cascade rig to directly relate geometry to the heat transfer rate, and Schobeiri and Lu [3], who proposed a method of physics based geometry generation using continuous diffusion.

1.1.1 Full function-based method

The first, "full function-based" method was initially proposed by Rose [4]. The endwalls were generated parametrically with a sinusoidal profile applied in the circumferential direction and a combination of a parabola and a sinusoid used in the axial direction. As the author noted, the approach is flawed as the aerofoil shape at the endwall is not preserved. However, if the vane has minimal radial stacking, any profile changes will be small.

The superposition of axisymmetric and non-axisymmetric shape functions was also used by Nagel and Baier [5]. The change in radius was defined in a rectangular domain by two functions, which resulted in approximately 15 parameters per endwall. A shape-defining function, prescribed between the suction and pressure surfaces, controlled the curvature in the circumferential direction. In the axial direction a decay function ensured that the change in radius was equal to zero at both the inlet and outlet of the row.

The parameterisation within a full function-based approach could be considered "object oriented" in the sense that various bumps, elevations, and depressions could be placed on the endwall. These features can be superposed and the amplitude, position, and shape individually adjusted. The advantage of this method is that it enables full control of the surface shape. The definition of shape in a rectangular domain before being transformed to a cascade domain simplifies the function and makes it robust to aerofoil shape, pitch, or chord changes. However, no details were provided in the open literature regarding how the geometry was transformed to the cascade test rig.

Saha and Acharya [6] also used a "full function-based" method by combining functions in the streamwise and pitchwise directions. Nine contoured endwalls were created by varying the streamwise profile while keeping the pitchwise curve constant.

1.1.2 Partially function-based method

The second, "partially function-based", method was demonstrated by Harvey et al. [7]. The authors extended the Forward And Inverse THree-dimensional (FAITH) design system for turbomachinery aerofoils and applied it to non-axisymmetric endwalls. The FAITH system was first described by Shahpar and Lapworth [8] and Shahpar et al. [9] and is based on linear perturbation theory.

The perturbation to the axisymmetric endwall surface was created by the product of two curves in the axial and circumferential directions. Six control stations were defined at specified axial distances along the mean camber line of the aerofoil. At each station a sinusoidal shape was generated in the circumferential direction using a three-term Fourier series. The height and phase angle of each wave can be specified by the user. The FAITH system was then used to fit a b-spline curve in the axial direction through each control station, creating 36 perturbations for each endwall; a surface was then fitted over the six b-splines to create the final geometry. Additional stations were then placed upstream and downstream in order to limit the axial extent of the profiling.

This method has certain advantages, including the circumferential area of the passage remaining constant, helping to limit throat errors, which is important for compressible flows. The general definition using sine and cosine functions is also helpful as the pressure field in the blade row is often of sinusoidal form. Also, in principle the summation of the first three terms in the Fourier series allow for almost any shape to be generated (only the first term was used in the published works).

1.1.3 Point-displacement method

The third method, termed "point-displacement", involves a set of control points defined along the blade passage controls 2-D cubic splines in both the pitch- and stream-wise directions. Each control point is given one degree of freedom, normal to the endwall.

The advantage of this method is that it is simple - any change in parameter results in a change in radial displacement.

Praisner et al. [10] used a matrix of 35 control points distributed across the endwall within a given upstream and downstream limit. Because this form of endwall parameterisation does not apply a periodic function in the pitch-wise direction, significant throat area variations can occur. In order to compensate for this, a throat-area correction scheme was incorporated by applying a function along the throat line. The form of this function can be arbitrary, however Praisner et al. [10] used a sinusoidal function to maintain the flow area. Other exponents of the "point displacement" method include Panchal et al.[11] ,Kim et al. [12], Tang et al. [13] and Lynch and Thole [14].

1.2 A general framework for EWC generation

Although each of the three established design approaches have similarities, there is scope to develop a new method that incorporates the advantages of each, while being robust enough to apply to any blade/vane geometry. Nagel and Baier [5] demonstrated it was possible to derive a method that provided unlimited control to produce any shape. However, this was only used in a cascade space and restricted the endwall profiling to the blade passage.

This paper presents a universal method for generating contoured endwalls. The generation method employs an adaptable meshing strategy, capable of being applied to any vane or blade, and a versatile function-based approach to defining the endwall shape. Section 2 is a review of the relevant literature concerning the use of endwall contouring in gas turbines. Section 3 describes the generation method for endwall contouring. Section 4 presents an application of the geometry generation framework, and the principal conclusions are given in Section 5.

2 REVIEW OF ENDWALL STUDIES

The following section presents a review of computational and experimental research identifying the benefit of applying endwall contouring in gas turbines. In each case the endwall generation method is compiled in Table 1, with reference to the location of the contouring, and determination of the shape-defining functions.

Publication	Method	Location of Contouring	Circumferential Profile	Axial Profile
Rose [4]	FFB	Passage and Aft Region	$f_p(Y) = \sin(N(Y - Y_{MC}) + C_2 + \frac{3\pi}{2} + C_1$ $C_3 = (X_{PTE} - X_{TE})\left(\tan(\beta) + \frac{1}{\tan(\beta)}\right)$ $C_2 = \frac{2\pi C_3}{\theta}$	$f_a(X) = \frac{Z_M}{2}\left(\sin\left(\pi\left(\frac{3}{2} - \left(\frac{X - X_{PTE}}{X_M - X_{PTE}}\right)\right)\right) + 1\right)$ $f_{a,PTE}(X) = \frac{2(X_{PTE} - X_M)^2}{Z_M \pi^2}$
Hartland *et al.* [15]	FFB	Passage and Aft Region	Same as [4]	Same as [4]
Harvey *et al.* [7]	PFB	All Regions	$f_p(Y) = \frac{1}{C_5}\sum_{i=1}^{3}\left(a_i \sin\left(\frac{2\pi Y}{\theta}\right) + b_i \cos\left(\frac{2\pi Y}{\theta}\right)\right)$	B-spline
Hartland *et al.* [16]	PFB	All Regions	$f_p(Y) = -X\cos(\pi(\frac{Y - Y_{MC}}{\theta}))$	Blade mean camber line, rotated then rescaled to fit blade axial chord then fillet fitted to both ends
Harvey *et al.* [20]	PFB	All Regions	Six axial control planes with fourier series	B-spline
Brennan *et al.* [18]	PFB	All Regions	Uses the FAITH system - 6 axial control planes with fourier series, 0-3rd order harmonics.	B-spline between control points
Nagel and Baier [5]	FFB	Passage Region	$Z(Y,X) = f_p(Y) \times f_a(X)$	2 Spline segments but also employs an axial decay function transformed from a rectangular domain
Reising and Schiffer [21]	PFB	All Regions	Four Bézier curves	Lofted surface
Germain *et al.* [22]	FFB	Passage Region	Continues the work by Nagel and Baier [5] using a circumferential function - half cosine or modified full cosine	Polynomial of sinusoidal functions
Torre *et al.* [24]	PFB	Fore and Passage Region	Three-term fourier series	Six axial control points
Praisner *et al.* [10]	PD	Passage Region	35 Control Points with splines in both directions, results in no perodicity at throat etc. so requires correcting factor	
Regina *et al.* [25]	PFB	All Regions	Fourier series for stator / B-spline for rotor	Lofted surface
Kim *et al.* [12]	PD	Passage Region	Refers to Praisner et al. [10]	
Tang *et al.* [13]	PD	All Regions	35 Control points with splines in both directions, results in no perodicity at throat etc. so requires correcting factor	
Lynch and Thole [14]	PD	Passage Region	Refers to Praisner et al. [10]	

Table 1 A summary of endwall generation methods applied in computational and experimental studies within the literature (FFB: Full Function-Based, PFB: Partially Function-Based, PD: Point Displacement)

One of the earliest applications of non-axisymmetric endwall contouring was demonstrated by Rose [3] to control the exit static pressure at the trailing edge platform of a High Pressure (HP) Nozzle Guide Vane (NGV). A sinusoidal profile was applied circumferentially to reduce the peak pressure at the rim seal gap between the vane and the rotor. By reducing the peak pressure, the turbine rim seal ingestion could be reduced. The basic principles of controlling the local static pressures by means of streamline curvature were established: the convex wall curvature locally accelerated the flow relative to the datum and thus reduced the static pressure, while concave curvature caused a (relative) diffusion, raising the static pressure. Computational Fluid Dynamics (CFD) was used to demonstrate a 70% reduction in pressure non-uniformities.

The most successful geometry from this study was then re-designed for a turbine rotor blade using CFD optimisation. It was tested by Hartland et al. [15] in a low speed linear cascade rig operating at an exit Mach number of 0.1, a Reynolds number of 4×105 and geometry representative of an HP rotor. The results showed good agreement with the CFD predictions, where the profiling was shown to accurately control the static pressure in the circumferential direction, but also demonstrated a small increase in secondary loss. It was noted however, that to have a larger effect on the secondary flow features, the contouring would have to be moved further upstream, near to where the secondary flow features are generated. Subsequently, there was a move towards implementing endwall contouring in the blade passage and using profiling to reduce secondary flow losses.

Harvey et al. [7] compared EWC to existing turbine design methods such as 'lean' and 'skew' of turbine blades, with the aim of reducing exit angle variations. The endwall design featured a circumferential sinusoidal perturbation, which peaked at the pressure surface near the leading edge of the aerofoil. Another sinusoid of lower amplitude was located further down the passage, with its peak towards the trailing edge of the suction

surface. The design reduced the cross-passage pressure gradient by creating streamline curvature in the radial direction. The cross-passage pressure gradient was considered to be the driving mechanism of secondary flows. Therefore, its reduction would lead to a reduction of Secondary Kinetic Energy (SKE) and endwall losses. The authors reported that their CFD simulations, performed with a mixing length turbulence model, did not reliably predict the reduction in loss associated with endwall contouring. They subsequently used predictions of cross-passage pressure gradient and SKE reduction to inform the design of endwalls.

The design of Harvey et al. [7] was then considered experimentally using the Durham cascade rig (Hartland et al. [16]). A net reduction in mixed out secondary loss of 34% was achieved, alongside a reduction in the exit angle deviation from the cascade. A counter vortex was found beneath the passage vortex which rotated in the opposite direction and reduced the overturning near the endwall. This was caused by the low pressure near the suction surface which was created by the convex curvature of the local profiling.

Hartland et al. [17] presented a simple method for the design of endwalls using the principle that the cross-passage pressure gradient can be cancelled out by mirroring the blade curvature on the endwall. Three endwall profiles were designed based on the camber line of the blade, with CFD used to predict a reduction in secondary flows for each case. The most successful design extended either side of the blades in an attempt to mitigate the issues associated with sharp curvature at inlet and exit of the blade row.

Brennan et al. [18] used the FAITH system to redesign the HP turbine of the Rolls-Royce Trent 500, using endwall contouring on both the vane and blade platforms. The design was predicted to reduce secondary losses by 0.4 % in total. Experimental validation was then conducted by Rose et al. [19] using a cold flow model test rig scaled to 76% of the Trent 500 HP turbine. The aerodynamic efficiency gain at engine representative conditions was 0.59% (±0.25%), exceeding the original prediction for the design. The benefits of endwall

profiling were also observed to be increased at turbine work and stage loading conditions above nominal design values. The authors noted that although the exit flow was more uniform, the secondary losses were kept closer to the endwalls; the change in the exit pressure field would have to be accounted for in the design of the downstream row. The same approach was taken by Harvey et al. [20] for the Trent 500 Intermediate Pressure (IP) turbine. This time the predicted reduction in secondary loss of 0.96 % was found to be 0.9 % (±0.4 %) in the experiment.

Nagel and Baier [5] used a transitional Navier-Stokes flow solver to perform a three-dimensional optimisation on turbine blades and endwalls to reduce losses. This study was unique in that it relied on total pressure loss predictions from the CFD as the objective function. A high-speed cascade rig was then used to validate the results which demonstrated a total pressure loss reduction of 22 % relative to the starting cascade.

Reising and Schiffer [21] conducted a numerical study on the benefits of using endwall contouring in an axial compressor. To parameterise the endwall, five cuts were defined, aligned with the mean camber line. Four axial locations were determined along each of the cuts, resulting in 16 parameters for the optimisation. Bezier curves controlled by the height parameters were used in the circumferential direction. The final process was a lofted surface passing through the perturbed cuts. The authors used an automated multi-objective optimiser connected to a 3D RANS flow solver to find the optimal endwall geometry. An increase in efficiency of 1.8% at the design condition was demonstrated due to the suppression of the hub-corner stall.

Germain et al. [22] continued the work of Nagel et al. [23] but modified the underlying mathematical functions in order to construct more complex and easily adjustable endwalls. A polynomial of sinusoidal functions was used for the axial decay function. The

efficiency of an experimental 1.5-stage axial turbine was shown to improve by 1% (±0.4%) through endwall contouring, although this was underestimated by the CFD.

Torre et al. [24] generated their endwall geometry by adding perturbations to the planar surface defined through a three-term Fourier series. The perturbations were specified at six axial locations. Experimental data confirmed that the contoured endwall achieved a reduction of 72% of SKEH and 20% of the mixed-out endwall losses. CFD results were used to illustrate the effect of the non-axisymmetric endwall on the secondary flows

Praisner et al. [10] applied non-axisymmetric endwall contouring to three turbine aerofoils, including two high-lift designs. Optimised designs were obtained by coupling CFD predictions with a free-form parameterisation of the endwall. Using a similar approach to Nagel and Baier [5], the objective function for the optimisation process was the predicted mass-averaged total pressure loss.

Regina et al. [25] used both steady and unsteady aerodynamic measurements to evaluate the aerodynamic performance of a turbine stage with EWC, with and without purge flow from the rim seal. They measured a 0.2% increase in efficiency with EWC but showed this was eliminated in the presence of significant purge flow. The authors noted that investing effort in a combined design of the EWC and the exit geometry of the rim seal is considered the best means of improving aerodynamic performance.

3 GENERATION METHOD

The aim of this paper is to present a Geometry Generation (GGF) for generating contoured endwalls. An adaptable meshing strategy is proposed, capable of applying contouring to any aerodynamic profile; a versatile function-based approach is then used to define the endwall shape. These two key components of the generation method will be discussed in this section.

3.1 Meshing

3.1.1. Full Platform Contouring

The cascade view offers a convenient way of visualising gas turbine vane and blade rows. It represents the vane/blade profile at a given radius as a plot of circumferential versus axial co-ordinates; this profile is repeated at pitch intervals in the circumferential direction to generate a plan view of the vane/blade row. In this paper, cascade views of the vane/blade profile at the hub endwall are constructed using dimensionless axial (X) and circumferential (Y) co-ordinates, as defined in Eqs. (1) and (2) below:

$$X = \frac{x}{C} \tag{1}$$

and

$$Y = \frac{r_h \theta}{P} \tag{2}$$

where x is the axial co-ordinate of the vane/blade profile at the hub radius. C is the axial chord of the vane/blade. r_h is the non-contoured hub endwall radius. θ is the azimuthal co ordinate of the vane/blade profile at the hub radius in radians and P is the vane/blade pitch at the hub, given by

$$P = \frac{2\pi r_h}{N} \tag{3}$$

where N is the total number of vanes/blades. The leading edge of the first vane/blade in the cascade is located at the origin of the (X, Y) co-ordinate system – annular co-ordinates x and θ must be appropriately referenced from the leading edge of the vane/blade. Given the definition of X in Eq. (1), the trailing edge of the vane/blade profile will be located at $X=1$. Subsequent blades in the cascade will have the same profile shape but with co-ordinates offset in the Y-direction by 1 relative to the previous profile.

Figure 2 shows a generic vane/blade profile plotted in the cascade view; a second vane/blade profile has been added to the view to form a passage between the two profiles.

Three distinct endwall regions are identified in the figure: the fore region, which extends axially upstream of the vane/blade leading edge; the passage region, which is bound by the leading and trailing edges and the modified mean camber lines of adjacent vanes/blades; and the aft region, which extends axially downstream of the vane/blade trailing edge. The extents to which the fore and aft regions extend axially upstream and downstream of the leading and trailing edges respectively are determined by the location of the fore and aft rim seals (Figure 1). For the first stage vane there is no upstream rim seal, and so the engine designer must manually define the extent to which the fore region extends axially upstream of the vane leading edge.

The modified mean camber lines were chosen to bound the mesh as this allows for greater control of the intersection with the pressure and suction surfaces of the vane/blade (this is taken up further in Section 3.2.1). The true camber lines were modified so that they tend to the geometric extent of the vane/blade at $X = 0$ and $X = 1$, i.e. spanning the full axial chord of the vane/blade. This modification prevents a disconnected region forming around the leading edge or trailing edge of the vane/blade profile. Figure 2 shows that the modified mean camber lines (shown as $g(X)$ and $f(X)$ for two adjacent blades) deviate from the true camber lines when $X \leq 0.1$ and $X \geq 0.9$. Third-order polynomials are used to blend the camber lines to the vane/blade co-ordinate at $X = 0$ and $X = 1$.
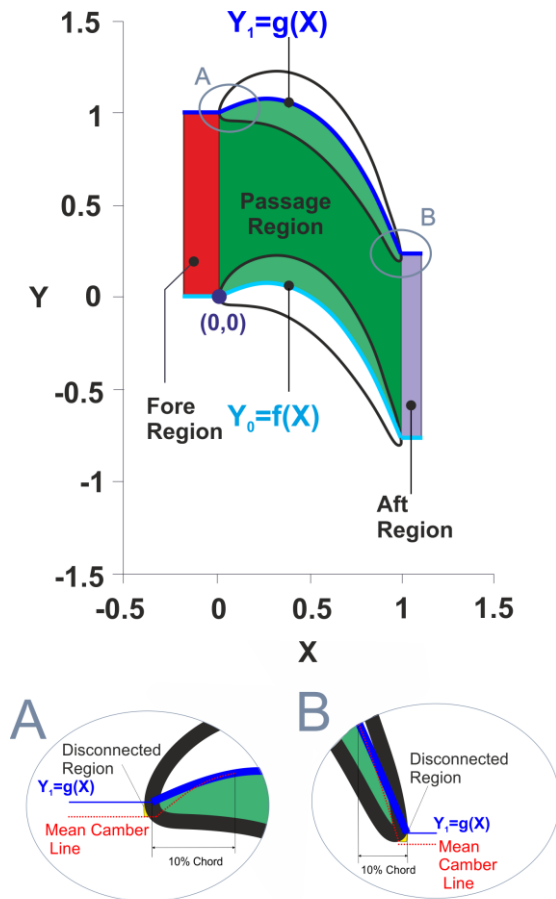
Figure 2 A cascade view of a generic vane/blade profile at the hub with endwall regions identified.

The contoured endwall mesh is defined by a series of functions that modify the shape of the 'baseline' non-contoured endwall mesh. An orthonormal baseline mesh simplifies the definition of these functions. The endwall regions highlighted in the cascade view in Fig. 2 can be represented orthonormally using a Cartesian co-ordinate system with axes (X, Y^*), with Y^* defined as:

$$Y^* = \frac{Y - Y_0}{Y_1 - Y_0} \tag{4}$$

where Y_0 and Y_1 are the values of Y at the lower and upper boundaries of the endwall regions, respectively, for a given value of X, as shown in Fig. 2. The orthonormal representation of the non-contoured endwall is subsequently shown in Fig. 3. Note: fixing the leading edge of

the first vane/blade in the cascade view at the origin of the (*X, Y*) co-ordinate system bounds

the orthonormally-represented passage region between $0 \le Y^* \le 1$ and $0 \le X \le 1$. This
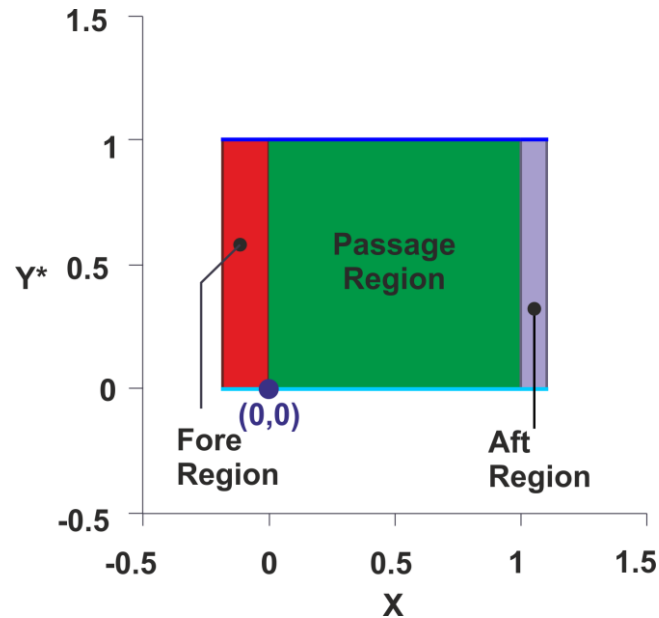
provides convenient limits for the contouring functions.

Figure 3 Orthonormal representation of a generic vane/blade endwall (XY* plane at Z = 0).

A regular grid can be used to discretise the three regions that form the orthonormally-

represented non-contoured endwall. There are two instances of shared boundaries between

regions: first, between the fore and passage regions at the leading edge; second, between the

passage and aft regions at the trailing edge. The three contiguous regions will share nodes at

these common boundaries – this requires matched grid spacing in the Y^*-direction. The grid

spacing in the X direction can be independently set in each of the three regions. Meshing the

endwall regions independently offers greater control over the contouring process than if a

universal mesh was used. Shape defining functions can be applied to each region, enabling

contouring to be selectively 'switched-off' (for example in the fore or aft regions). The

baseline orthonormal mesh is shown in Fig. 4(a). Conversion of this mesh back to the

cascade view is shown in Fig. 4(b), processed using the co-ordinate translation given in Eq. 4.

The orthonormal baseline mesh lies on the XY^* plane in the three-dimensional Cartesian co-ordinate space (X, Y^*, Z), with Z given by:

$$Z = \frac{r - r_h}{r_t - r_h} \qquad (5)$$

where r_h and r_t are the radii of the non-contoured endwall hub and vane/blade tip respectively. Note that $r_t - r_h$ is equal to the span (S) of the vane/blade.

The contoured endwall is defined by functions that shift the orthonormal baseline mesh nodes in the Z-direction (note: X and Y^* positions are maintained). The nodal co-ordinates of the orthonormal mesh are then translated between the (X, Y^*, Z) and (x, r, θ) co-ordinate systems using the following conversion:
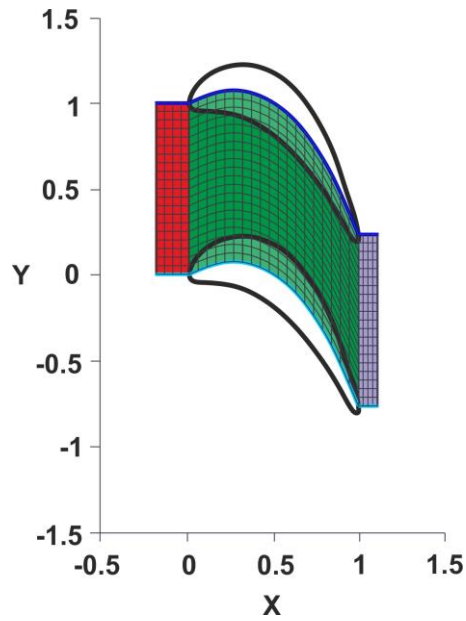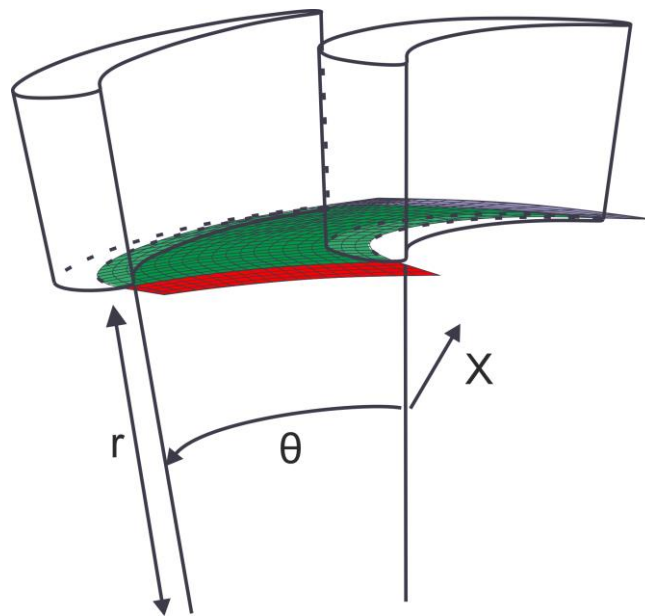
$$x = XC \qquad (6)$$

$$r = ZS + r_h \qquad (7)$$

$$\theta = [Y_0 + Y^*(Y_1 - Y_0)]\frac{P}{r_h} \qquad (8)$$
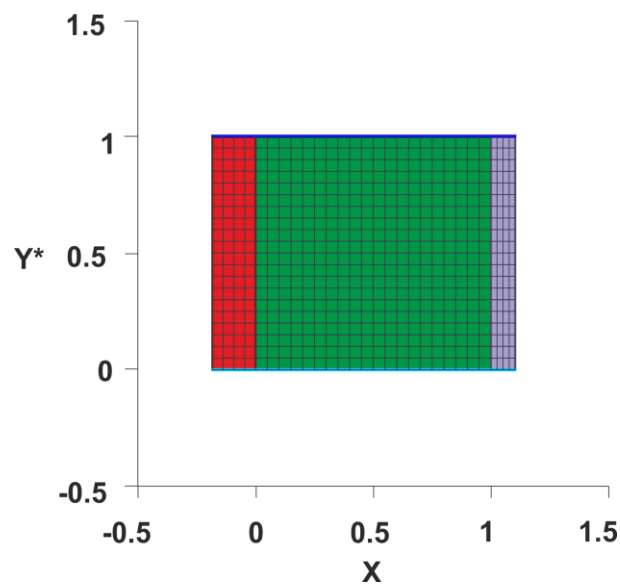

(a)

(b)

(c)

Figure 4 Baseline endwall mesh for a generic vane/blade profile: (a) orthonormal view; (b) cascade view; (c) polar view.

The conversion is shown graphically between Fig. 4(a) and Fig. 4(c). This provides a mesh for a contoured passage that can be repeated N times around the circumference to form the final contoured endwall platform.

3.1.2. Termination at the throat

The baseline orthonormal endwall mesh enables contouring across the entire axial extent of the stator/rotor platform, i.e. from the rim seal upstream of the leading edge to the rim seal downstream of the trailing edge. In some cases the engine designer will want to maintain the stage reaction between their non-contoured and contoured endwall designs, which will necessitate keeping the throat area fixed. The simplest way of achieving this is to remove the aft region mesh and to re-map the passage region mesh in the cascade view so that it terminates at the throat – functions can then be used to contour the endwall between the leading edge and throat. This method necessitates that downstream of the throat the endwall is non-contoured.
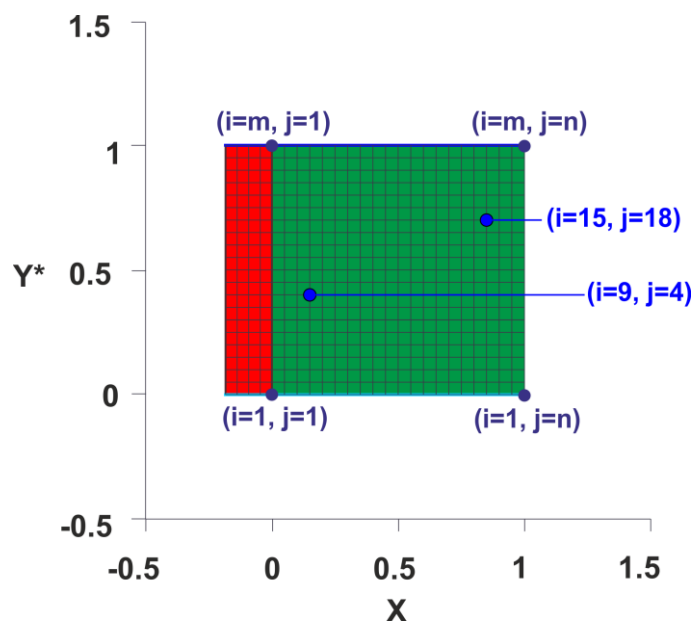
(a)
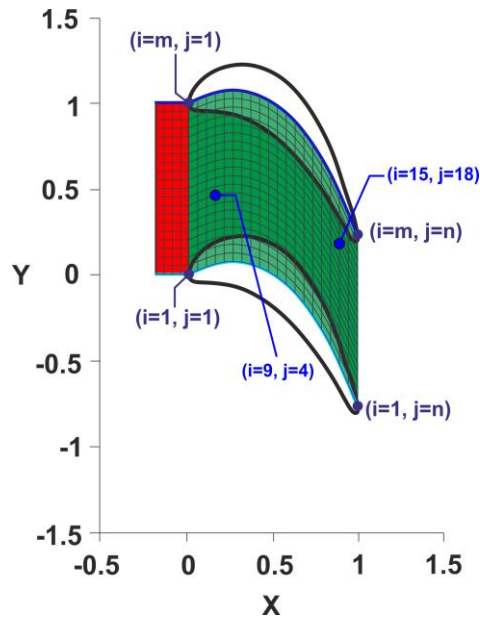
(b)

Figure 5 Baseline endwall passage region mesh for a generic vane/blade profile (a) orthonormal view and (b) cascade view. Nodal indices are marked at the corners of the meshes.

The passage region orthonormal mesh is a regular grid comprising m rows and n columns. Nodes can be conveniently indexed by row (i) and column (j) number, where $(i = 1, j = 1)$ is located at the lower left corner of the mesh and $(i = m, j = n)$ is located at the upper right corner of the mesh, as shown in Fig. 5(a). Nodal indices are maintained between the orthonormal and cascade meshes –Fig. 5(b) plots the corner node indices for the cascade mesh. Arbitrary nodes (and their indices) have also been plotted in Figs. 5(a) and (b) to demonstrate the transformation of nodes between the two co-ordinate systems.

The throat line, $Y = h(X, Y)$ (shown in Figure 6), is found by computing the shortest straight line between the pressure and suction surfaces of adjacent blades in the cascade view. This straight line is extended between the mean camber lines to provide a new boundary for the blade passage region, as shown in Fig. 6. The lower and upper mean camber lines are represented by functions $Y = f(X)$ and $Y = g(X)$ respectively. Third-degree polynomials were used for these functions in this paper. The points of intersection between

the mean camber lines and the throat line provides the location of the corner nodes at ($i =$ 1, $j = n$) and (i = m, j = n) for the re mapped passage region.
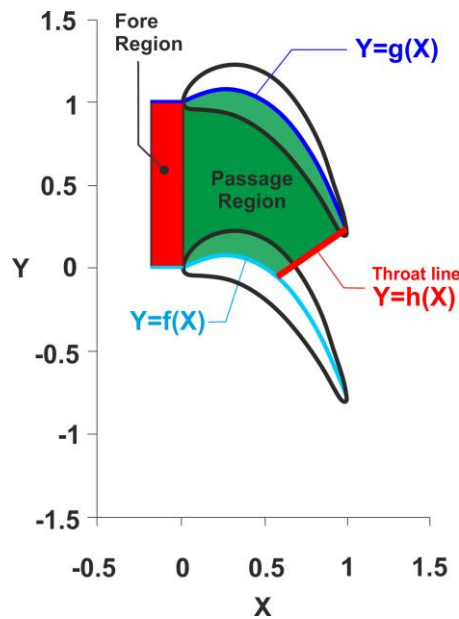

Figure 6 Passage region terminating at the throat.

Let $X_{i,j}$ and $Y_{i,j}$ denote the X and Y co-ordinates respectively of each node. For the lower mean camber line, $i = 1$ and so the X co-ordinates for the nodes distributed along the line can be written as.

$$\left(X_{1,j}\right)_{j=1}^{n} \tag{9}$$

Likewise, for the upper mean camber line, where i = m, the X co-ordinates for the nodes distributed along the line can be written as

$$\left(X_{m,j}\right)_{j=1}^{n} \tag{10}$$

Note that $X_{1,1} = X_{m,1} = 0$, $X_{1,n}$ is the X-co-ordinate at the point of intersection of the lower mean camber line and the throat line (i.e. where $f(X) = h(X)$) and $X_{m,n}$ is the X co-ordinate at the point of intersection of the upper mean camber line and the throat line (i.e. where $g(X) = h(X)$).

The length of the lower mean camber line between the leading edge and throat line can be calculated from

$$L_1 = \int_0^{X_{1,n}} \sqrt{1 + (f'(X))^2} \, dX \tag{11}$$

Similarly, the length of the upper mean camber line between the leading edge and throat line can be calculated from

$$L_m = \int_0^{X_{m,n}} \sqrt{1 + (g'(X))^2} \, dX \tag{12}$$

The n nodes along each of the mean camber lines will be distributed evenly between the leading edge and throat line. For the lower mean camber line the node spacing is given by

$$\Delta L_1 = \frac{L_1}{(n-1)} \tag{13}$$

and for the upper mean camber line it is given by

$$\Delta L_m = \frac{L_m}{(n-1)} \tag{14}$$

Thus for the jth node along the curves

$$F = (j-1)\Delta L_1 - \int_0^{X_{1,j}} \sqrt{1 + (f'(X))^2} \, dX = 0 \tag{15}$$

and

$$G = (j-1)\Delta L_m - \int_0^{X_{m,j}} \sqrt{1 + (g'(X))^2} \, dX = 0 \tag{16}$$

Hence the $(k+1)^{th}$ iterative values of $X_{1,j}$ and $X_{m,j}$ can be calculated from the following Newton-Raphson formulae

$$\left[\left(X_{1,j}\right)_{j=1}^{n}\right]_{k+1} = \left[\left(X_{1,j}\right)_{j=1}^{n}\right]_{k} - \frac{F}{F'} \tag{17}$$

and

$$\left[\left(X_{m,j}\right)_{j=1}^{n}\right]_{k+1} = \left[\left(X_{m,j}\right)_{j=1}^{n}\right]_{k} - \frac{G}{G'} \tag{18}$$

The corresponding *Y*-co-ordinates can be subsequently calculated from

$$\left(Y_{1,j}\right)_{j=1}^{n} = f\left(\left(X_{1,j}\right)_{j=1}^{n}\right) \tag{19}$$

and

$$\left(Y_{m,j}\right)_{j=1}^{n} = g\left(\left(X_{m,j}\right)_{j=1}^{n}\right) \tag{20}$$

Having found the *X* and *Y* co-ordinates for the nodes lying on the mean camber lines using Eqs. (17) – (20), the co-ordinates for nodes lying on rows $i = 2$ to $i = m - 1$ can be determined. Nodes must be distributed evenly along the straight lines that connect the jth nodes on the lower and upper mean camber lines. Hence linear interpolation can be used as follows

$$\left(\left(X_{i,j}\right)_{i=2}^{m-1}\right)_{j=1}^{n} = \left(X_{1,j}\right)_{j=1}^{n} + (j-1)\frac{\left(X_{m,j}\right)_{j=1}^{n} - \left(X_{1,j}\right)_{j=1}^{n}}{(m-1)} \tag{21}$$

and

$$\left(\left(Y_{1,j}\right)_{i=2}^{m-1}\right)_{j=1}^{n} = \left(Y_{1,j}\right)_{j=1}^{n} + (j-1)\frac{\left(Y_{m,j}\right)_{j=1}^{n} - \left(Y_{1,j}\right)_{j=1}^{n}}{(m-1)} \tag{22}$$

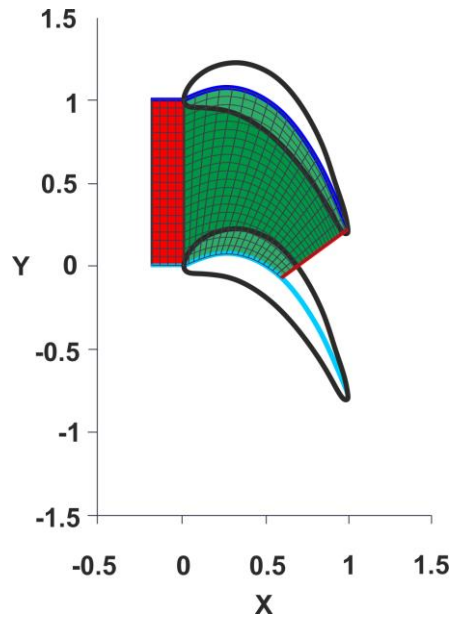The resulting re-distributed mesh is plotted in Fig. 7 for a generic blade profile.

Figure 7 Endwall mesh in the cascade domain for a generic vane/blade profile re-mapped to terminate at the throat.

3.2 Defining the endwall geometry – *full platform contouring*

With the mesh now created, the geometrical definition of the endwall contouring is specified in terms of mathematical functions. The method presented in this section concerns the generation of an endwall contour across the entire axial extent of the stator/rotor platform. A modified approach for the case where a mesh terminates at the vane/blade throat (introduced in Section 3.1.2) is presented in Appendix A.

3.2.1. Vane/blade profiles in the orthonormal plane

In order to improve control of the curvature at the blade-endwall intersection, the geometric functions are constrained between the suction-surface and pressure-surface of adjacent blades (i.e. the inter-blade passage). The first step is to identify blade intersection points at all relevant values of X, prescribed by the mesh density set in Section 3.1. By fitting a spline to the vane/blade profile, Y can be evaluated for all X. We will term these functions $\hat{g}(X)$ and $\hat{f}(X)$ for the pressure-surface and suction-surface part of the profile, respectively (shown in orange in Figure 8).

Simple geometric ratios are defined in order to transform the vane/blade intersection points back to the orthonormal domain. The distance in the Y-direction between the modified camber line and the profile suction-surface is termed $\Delta\widehat{Y}_0$ the distance between the modified camber line and the profile pressure surface is termed $\Delta\widehat{Y}_1$ (these values are shown in Figure 8).
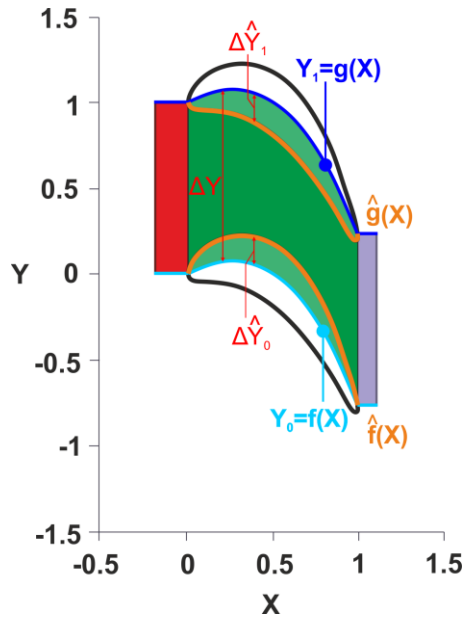

Figure 8 A cascade view of a generic blade profile identifying the blade-endwall intersections (note: the mesh lines have been omitted here for clarity).

The mathematical definitions of $\Delta\widehat{Y}_0$ and $\Delta\widehat{Y}_1$ are as follows:

$$\Delta\widehat{Y}_0 = \hat{f}(X) - f(X) \tag{23}$$

and

$$\Delta\widehat{Y}_1 = g(X) - \hat{g}(X) \tag{24}$$

Taking ΔY to be the pitch between adjacent vane/blade profiles, the geometric ratios are defined as follows:

$$\frac{\Delta Y}{\Delta\widehat{Y}_0} = \frac{\Delta Y^*}{\Delta\widehat{Y^*}_0} \tag{25}$$

and

$$\frac{\Delta Y}{\Delta \widehat{Y_1}} = \frac{\Delta Y^*}{\Delta \widehat{Y^*}_1}$$

(26)

where asterisks are used to distinguish the equivalent dimension in the orthonormal domain; these parameters are shown in Figure 9 (note that the functions are coloured equivalently to their representation in the cascade view in Figure 8).

In order to avoid discontinuities in gradient, or dislocations, in the endwall mesh, smoothing was used to blend the three regions together: the fore region to the passage region, and subsequently, the passage region to the aft region. The orthonormal domain shown in Figure 9 is reproduced in Figure 10, highlighting the discontinuities formed at the leading edge and trailing edge of the vane/blade. A function was used to smooth the intersections between $\hat{g}^*(X)$ and $g^*(X)$, both at the leading edge and trailing edge; similar polynomials were applied at the intersections between $\hat{f}^*(X)$ and $f^*(X)$. The smoothing function applied here was a third-order polynomial, however this is arbitrary, with the only requirement being that the smoothed curve remains inside the blade/vane profile.
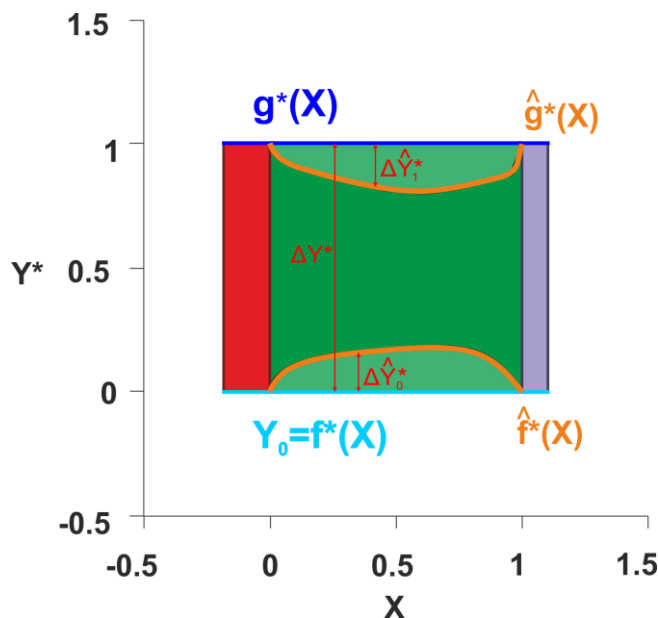

Figure 9 Representation of the vane/blade profile in the orthonormal domain (note: the mesh lines have been omitted here for clarity).

Figure 10 shows the smoothing curve used to connect $\hat{g}^*(X)$ and $g^*(X)$ at the leading edge of the vane/blade profile. The curve is created from the leading edge point and then intersects the profile on the pressure surface at 10% of the axial chord; at both ends of the curve the gradient tends to zero. This process is repeated for the three other discontinuities in the endwall mesh.
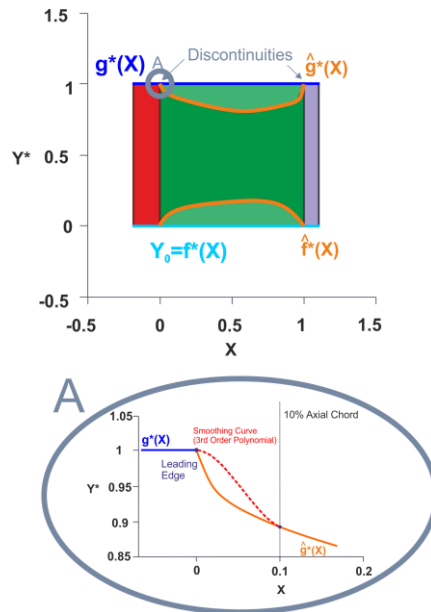

Figure 10 Smoothing curves used to avoid discontinuities in the mesh (note: the mesh lines have been omitted here for clarity).

It is worthy of note that when the shape functions for the endwall are defined (see Section 3.2.2), the smoothing regions (as shown in Figure 10) will intersect, and subsequently be subsumed by the vanes/blades when they are extruded through the endwall.

3.2.2. Rescaling the endwall contouring functions

Geometrically contoured endwalls are created by applying two types of shape-defining function: one in the pitch-wise direction, f_p, and one in the axial direction, f_a. These shape-defining functions are best visualised in the cascade space, shown in Figure 11.
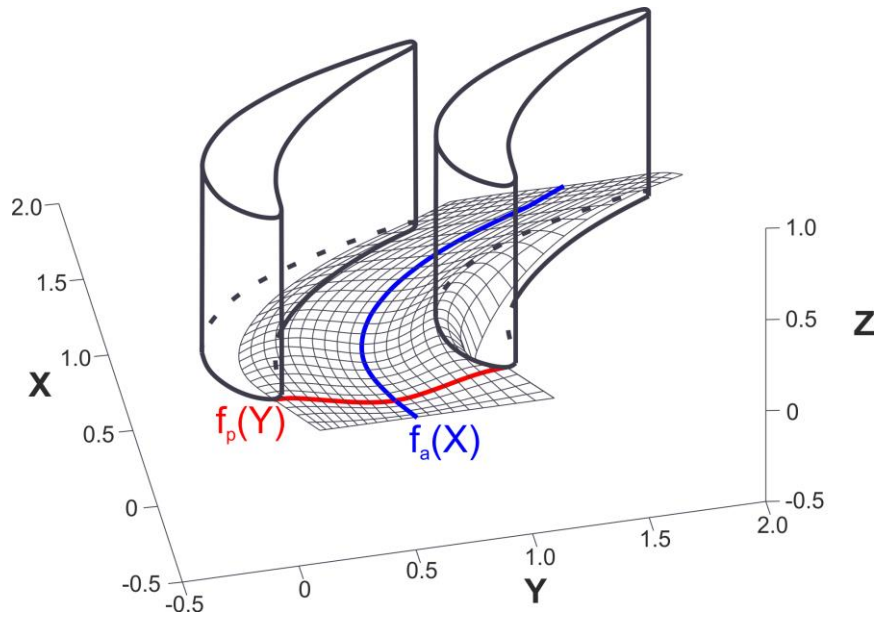
Figure 11 Use of two shape-defining functions for the creation of contoured endwall geometries (f_p shown in red, f_a shown in blue).

The Z co-ordinate (or radius of the endwall in ultimate terms) is therefore given as the product of the pitchwise and axial functions:

$$Z = f_p(Y) \cdot f_a(X) \tag{27}$$

When contoured endwalls are generated these functions (f_p and f_a) will be applied in the orthonormal domain; here f_p will be a function of the modified Y co-ordinate, Y^*.

In order that the functions are continuously bounded between 0 and 1 in the pitchwise direction, the inter-blade passage region is rescaled further; the fore and aft regions (see Figure 2), which are already bounded between zero and one by definition, match directly. The Y^* values are bounded using the following rescaling function:

$$\overline{Y^*} = \begin{cases} 1 & \text{when } X \leq 0 \\ \dfrac{Y^* - \widehat{f^*}(X)}{\widehat{g^*}(X) - \widehat{f^*}(X)} & \text{when } 0 < X < 1 \\ 1 & \text{when } X \geq 1 \end{cases} \tag{28}$$

where the vane/blade profiles are now represented in the orthonormal domain as shown in Figure 12 (shown in orange). This representation is a direct transformation from that shown in Figure 9.

The endwall shape is then given as:

$$Z^* = f_p(\overline{Y^*}) \cdot f_a(X) \tag{28}$$

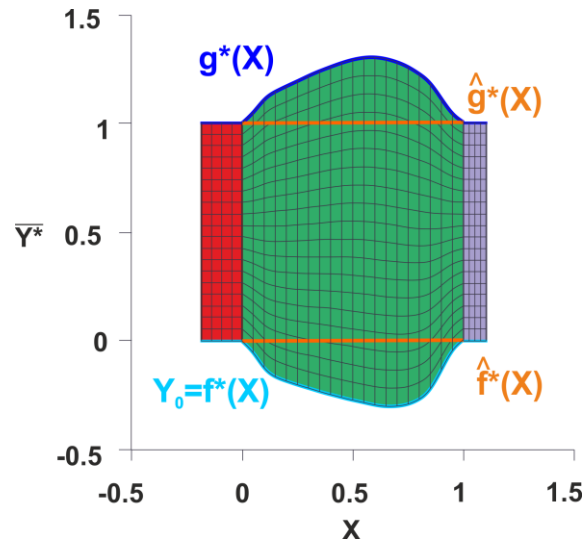where Z^* is the equivalent of Z in Eq. 27, transformed into the orthonormal domain.

**Figure 12 Representation of the vane/blade profile in the orthonormal domain using a rescaled $\overline{Y^*}$.**

Ultimately the definition of a contoured endwall depends on the selection of f_p and f_a. The orthonormal co-ordinate system featuring X, Y^* and Z^* is then used to define the endwall in three-dimensional space. Transformations from orthonormal to polar co-ordinates are then used to generate a part for manufacture; the applications of this geometry generation framework are taken up in Section 4.

## 4 APPLICATION OF THE GEOMETRY GENERATION FRAMEWORK

The endwall geometry generation framework presented here can be used to create any contoured shape. The mathematical formulae described in this paper were compiled in MATLAB and a Graphical User Interface (GUI) developed to generate contoured endwall

geometries (Figures 13-15). The process followed in applying the GGF can be summarised in the form of a flow-chart (Appendix B).

To demonstrate the user-controlled input to the programme, a simple endwall has been created using an axially-decaying sine-wave. Firstly, the meshing strategy described in Section 3.1 has been applied to a generic blade, including the fore, inter-blade and aft regions. An orthonormal representation of the mesh is shown in Figure 13(a).
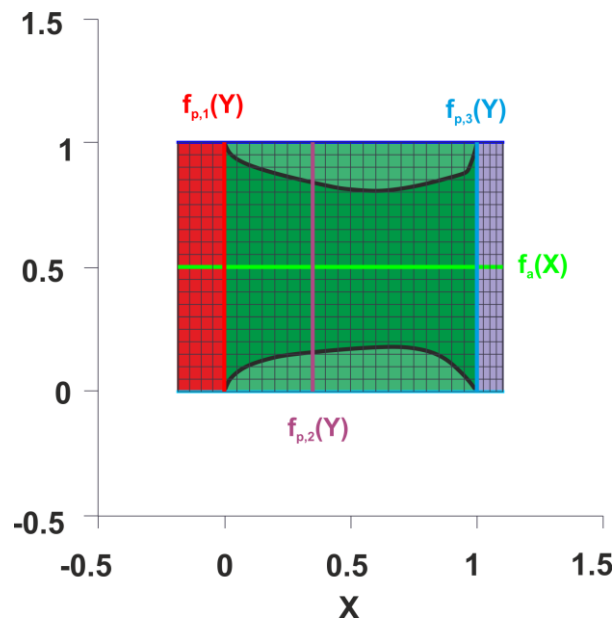
(a)
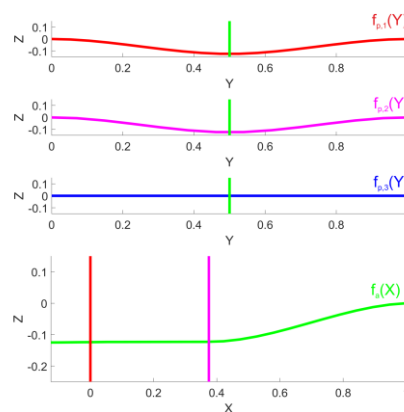
(b)

Figure 13 The generation of a simple endwall: (a) a generic blade profile and mesh shown in the orthonormal domain, (b) three pitchwise and one axial function used to define the endwall shape.

Three pitchwise functions, $f_{p,1-3}$, and a single axial function, f_a, have been selected (seen in Figure 13(a)). The form of each function is shown in Figure 13(b); the functions are colour-coded to show the intersections. Note that the choice of four control lines is arbitrary and it is dependent on the user to introduce additional control lines as the complexity of the contour geometry necessitates.
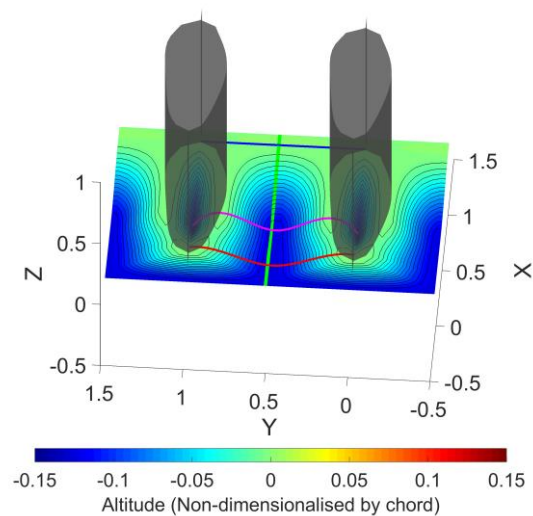

Figure 14 Orthonormal representation of the generated endwall surface.

Once the control lines are specified, the remaining mesh (in this case fifty rows and fifty columns) is populated by fitting third-order polynomials through the control lines. Note that the required mesh density is also dependent on the complexity of endwall curvature and is a user-specified input.

With a co-ordinate set for the endwall contour now defined, the endwall surface can be created for ease of visualisation by using the SURF function within MATLAB. An orthonormal representation of the complete endwall contour is shown in three dimensions (*X, Y*, Z*) in Figure 14.

The blades and endwall surface are then converted to the cascade domain using the conversions given in Section 3.1.1. The cascade representation of the endwall surface is shown in Figure 15.
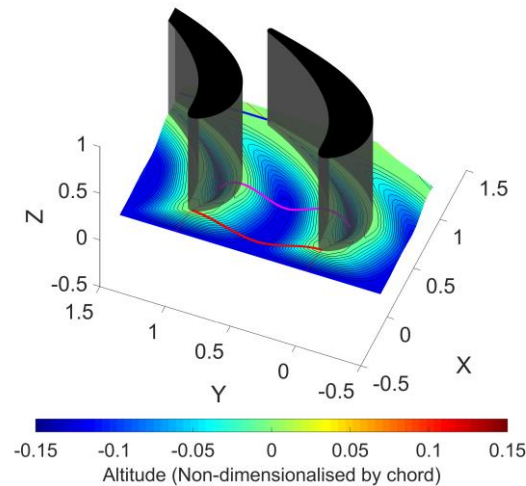

Figure 15 Cascade representation of the generated endwall surface.

The co-ordinates can be imported into a Computer-Aided Design (CAD) package and a loft feature, again, used to create a surface. Whether this loft process is possible over a grid of coordinate points is dependent on the CAD package employed by the user. If required by the CAD package, the coordinates can instead be extracted from MATLAB in the form of a series of high resolution circumferential curves; the surface can then be lofted over these curves. An alternate approach to the export process is to extract an STL file directly from MATLAB.

Once a surface has been generated, a fillet at the base of the vane/blade can be readily added using standard CAD processes.

4.1 Generation of endwalls from the literature

The robustness of the endwall geometry generation framework was demonstrated by re-creating endwalls from the literature. Three studies were selected based on their dissimilar

contouring styles: Chilla et al. [26] contoured the leading-edge region only, Regina et al. [25] contoured the inter-blade passage, while Hartland et al. [16] contoured the complete endwall. In each case the blade profile and platform geometry was digitized from the original article and the resulting endwall region was meshed automatically using the geometry generation framework presented in this paper. Each endwall shape was created using six pitchwise functions, $f_{p,1-6}$, and a single axial function, f_a; again, the number of control lines was selected based on the geometric complexity of the endwall shape. Each geometry was constructed using a 20x20 grid in each region; normally the grid resolution would be denser but this low resolution allowed the best visual comparison. The pitchwise functions contained a total of 35 free parameters for each geometry while the single axial function had a total of 6 free parameters; however, these numbers are completely arbitrary as they depend on the functions chosen.

The original endwalls from [26], [25] and [16] are reproduced in Figure 16 to aid direct comparison; the corresponding reproductions, created using the GGF, are shown immediately below each of the originals. The altitude of each endwall is shown with shaded contouring. The non-contoured altitude (i.e. that corresponding to a cylindrical endwall) is shown in green.
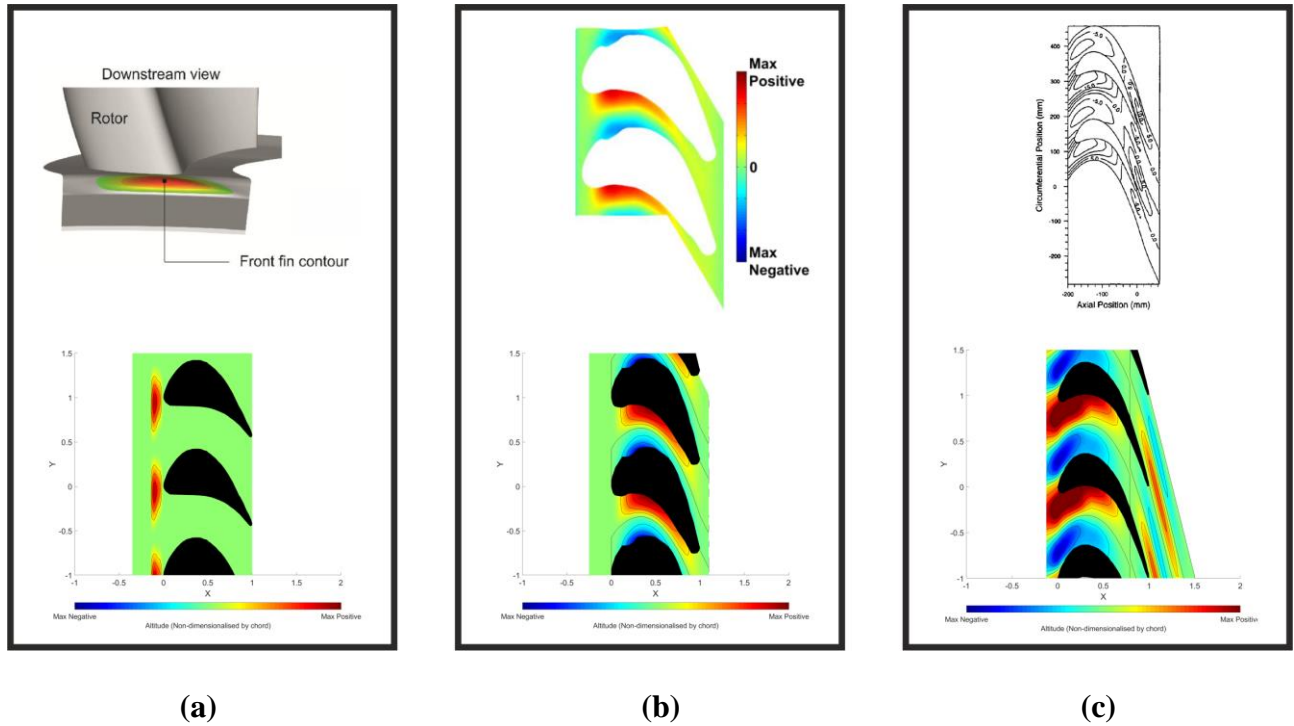
(a)   **(b)**   **(c)**

Figure 16 Use of the GDF to recreate endwalls from the literature: (a) a leading-edge feature [26], (b) an inter-blade passage contour [25], (c) fore, inter-blade and aft contour [16].

CONCLUSIONS

Three strategies for the design of endwalls were identified from the literature: point-displacement; partially function-based; and full function-based. Full function-based methods offer the greatest control over the surface, although the variation in curvature is often limited by the function prescribed in the method. A Geometry Generation Framework (GGF) has been developed here that provides a universal method for the generation of contoured endwalls.

- A meshing strategy has been established capable of digitizing a vane/blade geometry before translating the profile into an orthonormal domain. The mesh is separated into three distinct areas: the fore, inter-blade and aft regions.

- Shape-defining functions are applied to the mesh in the orthonormal domain, allowing for the control of complex surface curvature. The orthonormal domain allows for continuity of curvature across endwall regions.

- A co-ordinate transformation can be used to terminate the endwall contouring at the throat, returning to a cylindrical endwall downstream. This maintains the stage reaction.

- The contoured endwall definition is finally converted from cascade to polar co-ordinates for importing into a CAD software package.

- The versatility of the GGF is demonstrated by recreating endwalls from the literature; this includes a range of contouring styles across the fore, inter-blade and aft regions.

ACKNOWLEDGEMENTS

NOMENCLATURE

a,b Fourier series coefficients

C Chord (m)

C_1 Pitchwise phase parameter (rad)

C_4 Coefficient of parabola

C_5 Normalising coefficient

f, g Geometric functions of the modified mean camber lines of adjacent blades

f_a Shape-defining function in the axial direction

f_p Shape-defining function in the pitchwise direction

$\hat{f}$ Geometric function for the suction-surface profile of a vane/blade

$\hat{g}$ Geometric function for the pressure-surface profile of a vane/blade

h Geometric function of throat line

L Length of integral segment (m)

m	Number of mesh rows in orthonormal domain
N	Number of vanes/blades
n	Number of mesh columns in orthonormal domain
P	Vane/blade pitch at the hub (m)
r	Radius (m)
S	Span (m)
X	Dimensionless axial co-ordinate
X^*	X co-ordinate translated in to orthonormal domain
x	Axial co-ordinate of the vane/blade profile at the hub
Y	Dimensionless circumferential co-ordinate
Y^*	Y co-ordinate translated in to orthonormal domain
$\overline{Y^*}$	Rescaled pitch-wise co-ordinate between inter-blade passage
ΔY	Pitch-wise separation between the modified mean camber lines of adjacent vanes/blades
$\Delta \hat{Y}_0$	Distance in Y-direction between the modified camber line and the vane/blade suction-surface
$\Delta \hat{Y}_1$	Distance in Y-direction between the modified camber line and the vane/blade pressure-surface
Z	Dimensionless spanwise co-ordinate
Z^*	Z co-ordinate translated in to orthonormal domain
β	Vane exit angle in absolute frame
θ	Azimuthal co-ordinate of the vane/blade profile at the hub

Subscripts

h	Root of vane/blade
LE	Aerofoil leading-edge

M	Location of maximum endwall altitude
MC	Mean camber
PTE	Platform trailing-edge
TE	Aerofoil trailing-edge
t	Tip of vane/blade
0	Value at the lower bound of the endwall mesh
1	Value at the upper bound of the endwall mesh

Superscripts

$*$	*Indicative of a co-ordinate in the orthonormal domain*
$'$	*Derivative*

REFERENCES

[1] Takeishi, K., Matsuura, M., Aoki, S. and Sato, T, 1990, "An Experimental Study of Heat Transfer and Film Cooling on Low Aspect Ratio Turbine Nozzles," ASME J. Turbomach., 112 (3), 488-496.

[2] Haase, K., Winkler, S., Weigand, B. and Neumann, S. O., 2012, "Novel Turbine Endwall Contours for the Reduction of Heat Transfer Generated using Ice Formation Method," ASME Paper No. IMECE2012-87430

[3] Schobeiri, M. T. and Lu, K., 2011, "Endwall Contouring using Continuous Diffusion, A Breakthrough Method and its Application to a Three-Stage High Pressure Turbine," ASME Paper No. GT2011-45931

[4] Rose, M. G, 1994, "Non-Axisymmetric Endwall Profiling in the HP NGV's of an Axial Flow Gas Turbine," ASME Paper No. 94-GT-249.

[5] Nagel, M. G. and Baier, R., 2005, "Experimentally Verified Numerical Optimization of a Three-Dimensional Parameterized Turbine Vane with Non-Axisymmetric End Walls," ASME J. Turbomach., 127 (2), 380-387.

[6] Saha, A. K. and Acharya, S., 2006, "Computations of Turbulent Flow and Heat Transfer Through a Three-Dimensional Non-Axisymmetric Blade Passage," ASME Paper No. GT2006-90390

[7] Harvey, N. W., Rose, M. G., Taylor, M. D., Shahpar, S., Hartland, J. C. and Gregory-Smith, D. G., 2000, "Non-Axisymmetric Turbine End Wall Design: Part 1 Three-Dimensional Linear Design System," ASME J. Turbomach., 122 (2), 278-285.

[8] Shahpar S., Lapworth B. L., 1998, "A Forward and Inverse Three-Dimensional Linear Design System for Turbomachinery Applications", 4th ECCOMASS Computational Fluid Dynamics Conference, Athens 7-11 September.

[9] Shahpar S., Lapworth B. L., De Pablos T., Taylor M. D., 1999, "A Linear Approach to the Multi-Parameter Design of Three-Dimensional Turbomachinery Blades", AIAA 99-0363.

[10] Praisner, T. J., Allen-Bradley, E., Grover, E. A., Knezevici, D. C. and Sjolander, S. A., 2013, "Application of Nonaxisymmetric Endwall Contouring to Conventional and High-Lift Turbine Airfoils," ASME J. Turbomach., 135 (6), 061006.

[11] Panchal, K., Abraham, S., Ekkad, S. V., Ng, W., Brown, B. J. and Malandra, A., 2011, "Investigation of Effect of End Wall Contouring Methods on a Transonic Turbine Blade Passage" ASME Paper No. GT2011-45192

[12] Kim, I., Kim. J., Cho, J. and Kang, Y., 2016, "Non-Axisymmetric Endwall Profile Optimization of a High-Pressure Transonic Turbine Using Approximation Model," ASME Paper No. GT2016-57970.

[13] Tang, H., Liu, S. and Luo, H., 2016, "Design Optimization of Profiled Endwall with Consideration of Cooling and Rim Seal Flow Effects," ASME Paper No. GT2016-57219.

[14] Lynch, S. P. and Thole, K. A., 2016, "Comparison of Three-Dimensional Boundary Layer on Flat versus Contoured Turbine Endwalls," ASME J. Turbomach., 138 (4), 041008.

[15] Hartland, J. C., Gregory-Smith, D. G. and Rose, M. G., 1998, "Non-Axisymmetric Endwall Profiling in a Turbine Rotor Blade," ASME Paper No. 98-GT-525.

[16] Hartland, J. C., Gregory-Smith, D. G., Harvey, N. W. and Rose, M. G., 2000, "Non-Axisymmetric Turbine End Wall Design: Part 2 Experimental Validation," ASME J. Turbomach., 122 (2), 286-293.

[17] Hartland, J. C. and Gregory-Smith, D. G., 2002, "A Design Method for the Profiling of End Walls in Turbines," ASME Paper No. GT-2002-30433.

[18] Brennan, G., Harvey, N. W., Rose, M. G., Fomison, N. and Taylor, M. D., 2003, "Improving the Efficiency of the Trent 500-HP Turbine using Nonaxisymmetric End Walls - Part 1: Turbine Design," ASME J. Turbomach., 125 (3), 497-504.

[19] Rose, M. G., Harvey, N. W., Seaman, P., Newman, D. A. & McManus, D., 2001, "Improving the Efficiency of the Trent 500-HP Turbine using Non-Axisymmetric End Walls Part 2: Experimental Validation," ASME Paper No. 2001-GT-0505.

[20] Harvey, N. W., Brennan, G., Newman, D. A. and Rose, M. G., 2002, "Improving Turbine Efficiency using Non-Axisymmetric End Walls: Validation in the Multi-Row Environment and with Low Aspect Ratio Blading," ASME Paper No. GT-2002-30337.

[21] Reising, S. and Schiffer, H.P., 2009, "Non-Axisymmetric End Wall Profiling in Transonic Compressors—Part I: Improving the Static Pressure Recovery at Off-Design Conditions by Sequential Hub and Shroud End Wall Profiling," ASME Paper No. GT2009-59133.

[22] Germain, T., Nagel, M., Raab, I., Schupbach, P., Abhari, R. S. and Rose, M. G., 2010, "Improving Efficiency of a High Work Turbine Using Nonaxisymmetric Endwalls— Part I: Endwall Design and Performance," ASME J. Turbomach., 132 (2), 021007.

[23] Nagel, M., Fottner, L., and Baier, R.-D., 2001, "Optimization of Three Dimensionally Designed Turbines Blades and Side Walls," ISABE Paper No. 2001-1058.

[24] Torre, D., Vazquez, R., de la Rosa Blanco, E., and Hodson, H. P., 2011, "A New Alternative for Reduction in Secondary Flows in Low Pressure Turbines," ASME J. Turbomach., 133 (1), 011029.

[25] Regina, K., Kalfas, A. I., Abhari, R. S., Lohaus, A. S., Voelker, S. & Kampe, T. A. D., 2014. "Aerodynamic Robustness of End Wall Contouring Against Rim Seal Purge Flow," ASME Paper No. GT2014-26007.

[26] Chilla, M., Hodson, H.P., Pullan, G. & Newman, D., 2016, "High Pressure Turbine Rim Seal Design for Increased Efficiency," ASME Paper No. GT2016-57495.

APPENDIX A: VANE/BLADE PROFILES WITH MESH TERMINATION AT THE THROAT

As stated in Section 3.2.1, in order to improve control of the curvature at the blade-endwall intersection, the geometric functions were constrained between the suction-surface and pressure-surface of adjacent blades (i.e. the inter-blade passage). However, the method prescribed in Section 3.2.1 cannot be used for a mesh which has been terminated at the throat. This is due to the fact that as $X_{i,j}$ changes with i, the value of X also increases; with a mesh that does not terminate at the throat, as $X_{i,j}$ changes with i the value of X is constant.

Nodes must be distributed evenly along the straight lines that connect the jth nodes on the lower and upper mean camber lines (as discussed in Section 3.1.2). The re-mapped mesh lines (shown in Figure 7) are now non-parallel to the Y-axis. Pythagoras' Theorem must be used to determine the separation distances between the modified camber lines and their separation from the profile suction-surface and pressure-surfaces; these distances are termed $\Delta Y, \Delta \hat{Y}_0$ and $\Delta \hat{Y}_1$, respectively (see Figure A1). The profile functions, $\hat{g}(X)$ and $\hat{f}(X)$, can be found using the method presented in Section 3.2.1
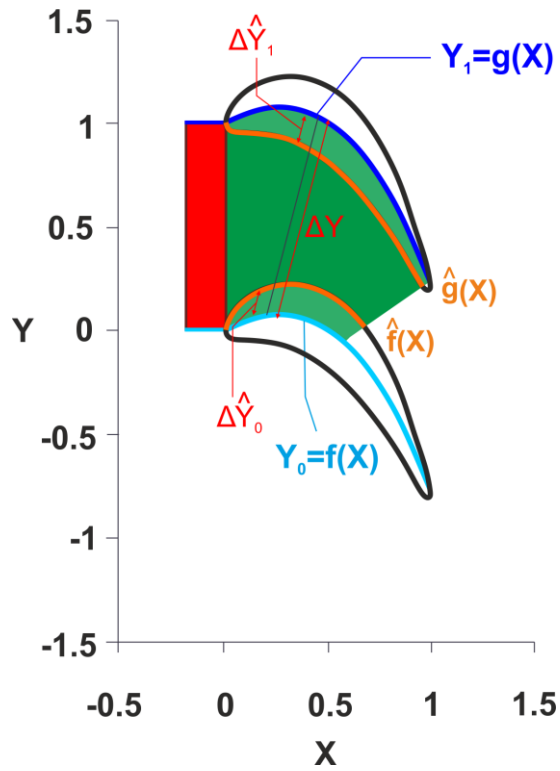
Figure A1: A cascade view of a generic blade profile identifying the blade-endwall intersections for an inter-blade passage mesh that terminates at the throat (note: the mesh lines have been omitted here for clarity)

Equations 23-26 can be used to convert the Y co-ordinate of the vane/blade profile to the orthonormal domain (designated subsequently by Y^*). Owing to the non-parallel nature of the re-mapped mesh when terminating at the throat, the X co-ordinates of the mesh and vane/blade profiles must also be converted to an orthonormal co-ordinate, X^*:

$$\left(\left(X^*_{i,j}\right)^m_{i=1}\right)^n_{j=1} = \frac{i-1}{n-1} \tag{A1}$$
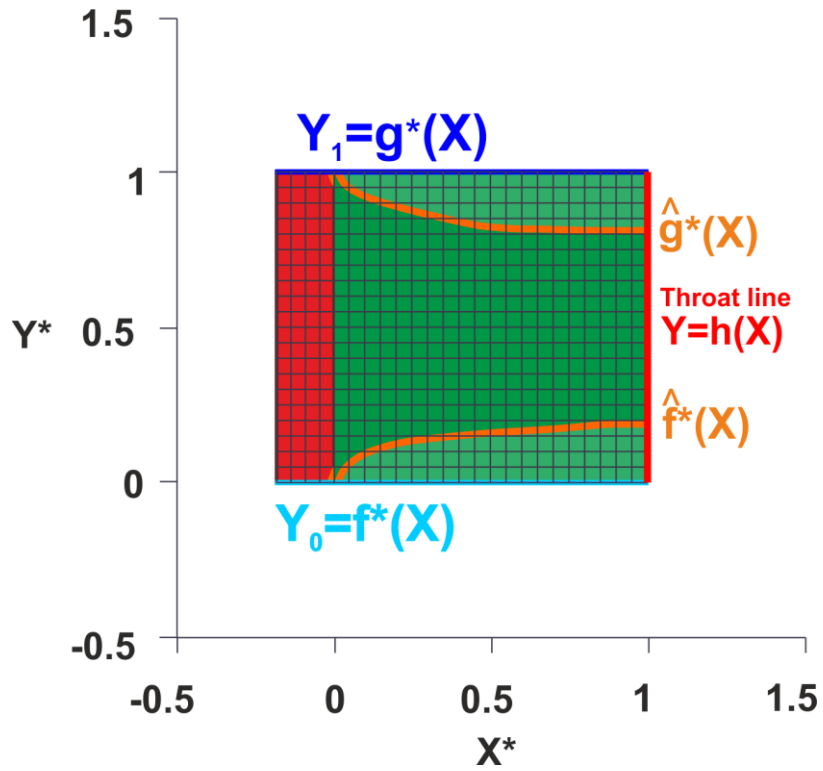
Figure A2: Endwall mesh in the orthonormal domain for a generic vane/blade profile re-mapped to terminate at the throat.

No further transformation is required in the fore region, where the rectangular grid is simply translated directly to the orthonormal domain according to Eqs. A2 and A3:

$$\left(\left(X^*_{i,j}\right)_{i=1}^{m}\right)_{j=1}^{n} = \left(\left(X_{i,j}\right)_{i=1}^{m}\right)_{j=1}^{n} \tag{A2}$$

and

$$\left(\left(Y^*_{i,j}\right)_{i=1}^{m}\right)_{j=1}^{n} = \left(\left(Y_{i,j}\right)_{i=1}^{m}\right)_{j=1}^{n} \tag{A3}$$

Note that X^* has been introduced when terminating at the throat in order that a rectangular grid occurs in the orthonormal domain (Figure A2); the rectangular grid is compatible with the method discussed in Section 3.2 for defining a contoured endwall geometry, where X and X^* are interchangeable.
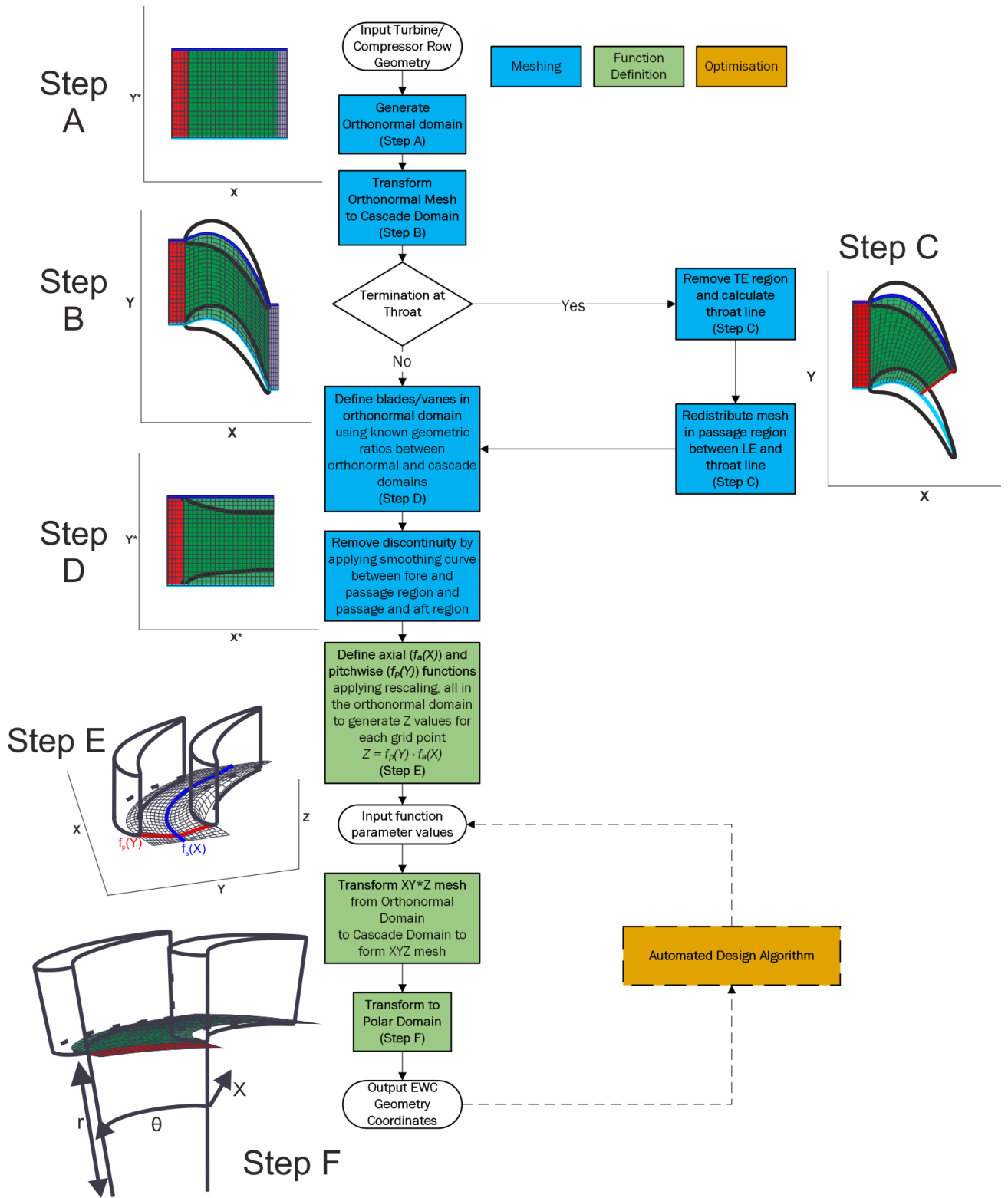
Figure B1: The process followed when employing the GGF, shown in the form of a flow-chart.